

The Electron Injection Spectrum Determined by Anomalous Excesses in Cosmic Ray, Gamma Ray, and Microwave Data

Tongyan Lin,^{1,2,*} Douglas Finkbeiner,^{1,2} and Gregory Dobler³

¹*Harvard-Smithsonian Center for Astrophysics, 60 Garden St., Cambridge, MA 02138, USA*

²*Physics Department, Harvard University, 17 Oxford St., Cambridge, MA 02138, USA*

³*Kavli Institute for Theoretical Physics, Kohn Hall, Santa Barbara, CA 93106, USA*

(Dated: May 10, 2022)

Recent cosmic ray, gamma ray, and microwave signals observed by Fermi, PAMELA, and WMAP indicate an unexpected primary source of e^+e^- at 10-1000 GeV. We fit these data to “standard backgrounds” plus a new source, assumed to be a separable function of position and energy. For the spatial part, we consider three cases: annihilating dark matter, decaying dark matter, and pulsars. In each case, we use GALPROP to inject energy in log-spaced energy bins and compute the expected cosmic-ray and photon signals for each bin. We then fit a linear combination of energy bins, plus backgrounds, to the data. We use a non-parametric fit, with no prior constraints on the spectrum except smoothness and non-negativity. In addition, we consider arbitrary modifications to the energy spectrum of the “ordinary” primary source function, fixing its spatial part, finding this alone to be inadequate to explain the PAMELA or WMAP signals. We explore variations in the fits due to choice of magnetic field, primary electron injection index, spatial profiles, propagation parameters, and fit regularization method. Dark matter annihilation fits well, where our fit finds a mass of ~ 1 TeV and a boost factor times energy fraction of ~ 70 . While it is possible for dark matter decay and pulsars to fit the data, unconventionally high magnetic fields and radiation densities are required near the Galactic Center to counter the relative shallowness of the assumed spatial profiles. We also fit to linear combinations of these three scenarios, though the fit is much less constrained.

I. INTRODUCTION

Several apparent anomalies in recent astrophysical data hint at a new source of high energy electrons, positrons, and possibly gamma rays, at the 10 GeV to 1 TeV scale. The cosmic ray signals observed by Fermi [1–4] and PAMELA [5] are direct evidence for these energetic electrons and positrons (e^+e^-), which would lose their energy primarily through synchrotron radiation and inverse Compton scattering (IC). If the number density of these e^+e^- rises towards the Galactic Center (GC), then this synchrotron and IC could explain the WMAP microwave “haze” [6] and the Fermi diffuse gamma ray “haze” [7], respectively.

It is difficult to explain these signals within the conventional diffusive propagation model and with standard assumptions about the interstellar medium (ISM). In this framework, the positron signal arises from secondary production from spallation of proton cosmic rays on the ISM. Assuming that 1. positrons and electrons have the same energy losses, 2. primary electrons and protons have the same production spectrum, and 3. the proton escape time decreases with energy, then the predicted positron fraction generically falls with energy, in contrast to the rising fraction observed by PAMELA. Katz et al. [8] point out these assumptions can be wrong, and explore alternative scenarios. Indeed, secondary production at shock fronts could explain the e^+ excess [9, 10], but this would also imply an excess of anti-protons, which is not observed. We will not consider these alternatives further.

We examine here whether a new primary source of e^+e^- is a viable explanation of the signals. First, the rise in the positron fraction measured by PAMELA suggests the presence of a new hard source of positrons [11]. Second, the WMAP “haze” is consistent with a hard synchrotron signal in the inner galaxy, in addition to a soft-spectrum synchrotron component traced by Haslam. Though this decomposition is not unique, it is a good fit to the WMAP data. Third, the Fermi gamma ray “haze” similarly extends to $|b| > 30^\circ$ above and below the plane in the inner galaxy. Neither haze correlates with the morphology of any known astrophysical objects or the ISM. (See Fig. 1.)

Many attempts to explain the data operate by including a new component of high energy particles and gamma rays originating from one of the following sources:

1. Annihilation of TeV-scale dark matter,
2. Decay of TeV-scale dark matter, or
3. An astrophysical source such as pulsars.

These sources can produce energetic electrons, positrons, and gamma rays. In addition, the dark matter distribution in the Galaxy is expected to be roughly spherical, providing at least qualitative agreement with the morphology of the gamma-ray and microwave haze. Nevertheless, each explanation above has drawbacks.

While annihilating dark matter may seem natural given a weak-scale WIMP which has a thermal freeze-out annihilation cross section, this vanilla scenario cannot explain the observed signals. Boost factors in the annihilation rate, arising from substructure or particle physics

* tongyan@physics.harvard.edu

	K_0 [kpc ² /Myr]	δ	L [kpc]
Default	0.097	0.43	4
M1	0.0765	0.46	15
MED	0.0112	0.70	4
M2	0.00595	0.55	1

TABLE I. Typical propagation parameters consistent with low-energy cosmic ray data [32]. We use the “Default” parameters and show the effect of using M1 and MED in Fig 5.

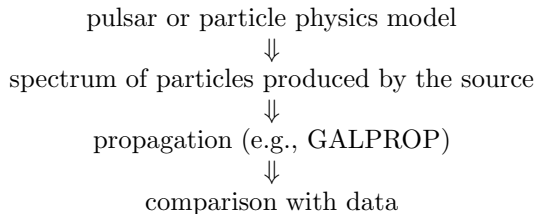
enhancement, of order 100-1000 are typically needed, depending on the annihilation channels and dark matter mass. Significant model-building effort is also required to explain the lack of excess in the observed \bar{p}/p flux [12]. For examples, see [13–17].

In the decaying dark matter scenario, dark matter has the freeze-out annihilation cross section but also decays with lifetime $\tau_\chi \sim 10^{26}$ s. These models also must explain why there is no excess in \bar{p}/p , though no boost factors are required. Examples include [18–24].

The pulsar explanation is the least exotic, but there are significant astrophysical uncertainties in pulsar distributions and e^+e^- emission spectra. The Fermi cosmic ray signals can be explained by the presence of one or more nearby pulsars with hard e^+e^- emission spectra [25–29]. However, pulsars are generally expected to be concentrated in the disk and it can be difficult to explain the shape of the WMAP and Fermi “haze” signals, which are much more spherical. See also [30, 31].

In this paper we quantify how well each of these three scenarios can explain the data described above without resorting to model-dependent details of the particle physics or pulsars. Rather we use the data to determine the best-fit injection spectrum of electrons and positrons produced by each new source. We also show that a simple modification to the background electron injection can explain the Fermi $e^+ + e^-$ spectrum and the Fermi gamma ray spectrum but not the rest of the data.

The standard procedure to analyse whether a model can explain the astrophysical signals is:



Often, one fits a specific dark matter or pulsar model to a subset of the “anomalous” signals described above. For dark matter, the particle physics model is usually processed through Pythia [33] to generate a spectrum of e^+e^- . The injection spectrum is the spectrum of e^+e^- produced per unit source times the rate of production of e^+e^- per source and the spatial distribution of the source. These injected e^+e^- are propagated through the Galaxy to obtain a steady-state solution. The signals are

then compared with data.

While some analyses have studied the cases above in a less model-dependent way, the injection spectrum is assumed to have one of a few common forms [16, 34, 35].

In this paper we effectively reverse the arrows in the procedure above. We fit the data from Fermi, PAMELA, and WMAP to expected backgrounds plus a new source which produces positrons and electrons. We assume the injection of the new source is separable in position and space. Rather than specifying the spectrum of e^+e^- injected by the new source, we fit for this injection spectrum as a function of energy. The shape of the spectrum is the same everywhere, and the spatial distribution is varied over several conventional models. Therefore, for our purposes, the three scenarios listed above differ only in their spatial distributions.

In the pulsar case, the assumption that the pulsar injection is a separable function of position and energy is a crude approximation that allows us to fit the data without specifying the details of pulsar physics, since the position dependence of pulsar populations and their e^+e^- injection spectra is very uncertain.

In our fits of the injection spectra, we simultaneously account for possible variations in the conventionally assumed spectrum and spatial distribution of the background injected electrons, as well as propagation parameters, magnetic field, and starlight densities. This takes into account the uncertainties in current models of the Galactic backgrounds.

We describe the signals and their expected backgrounds in more detail in the next section. We then present the overall framework of the analysis. Predictions are computed using GALPROP, and we allow for variations in the background model. We then present the best-fit injection spectrum for each of the three scenarios above, as well as the best-fit of the data to an arbitrary modification of the background electron injection spectrum. Finally we present injection spectra for linear combinations of these scenarios.

II. SIGNALS

In this section we review the method of computing the signals and standard assumptions made in modeling the astrophysical backgrounds. However, in our fits we allow for variations in many of these assumptions. This is discussed in more detail in Sec. III A.

In the conventional diffusive propagation model, the e^- cosmic ray density, $dn(\vec{x}, E)/dE$, is the steady-state solution to the diffusion and energy loss equation:

$$\begin{aligned}
 \frac{\partial}{\partial t} \left(\frac{dn(\vec{x}, E)}{dE} \right) &= 0 \\
 &= \vec{\nabla} \cdot \left[K(E) \vec{\nabla} \frac{dn}{dE} \right] + \frac{\partial}{\partial E} \left[b(E, \vec{x}) \frac{dn}{dE} \right] + Q(E, \vec{x})
 \end{aligned} \tag{1}$$

where the first term represents diffusion, the second term energy loss, and the third term the source term. $K(E)$

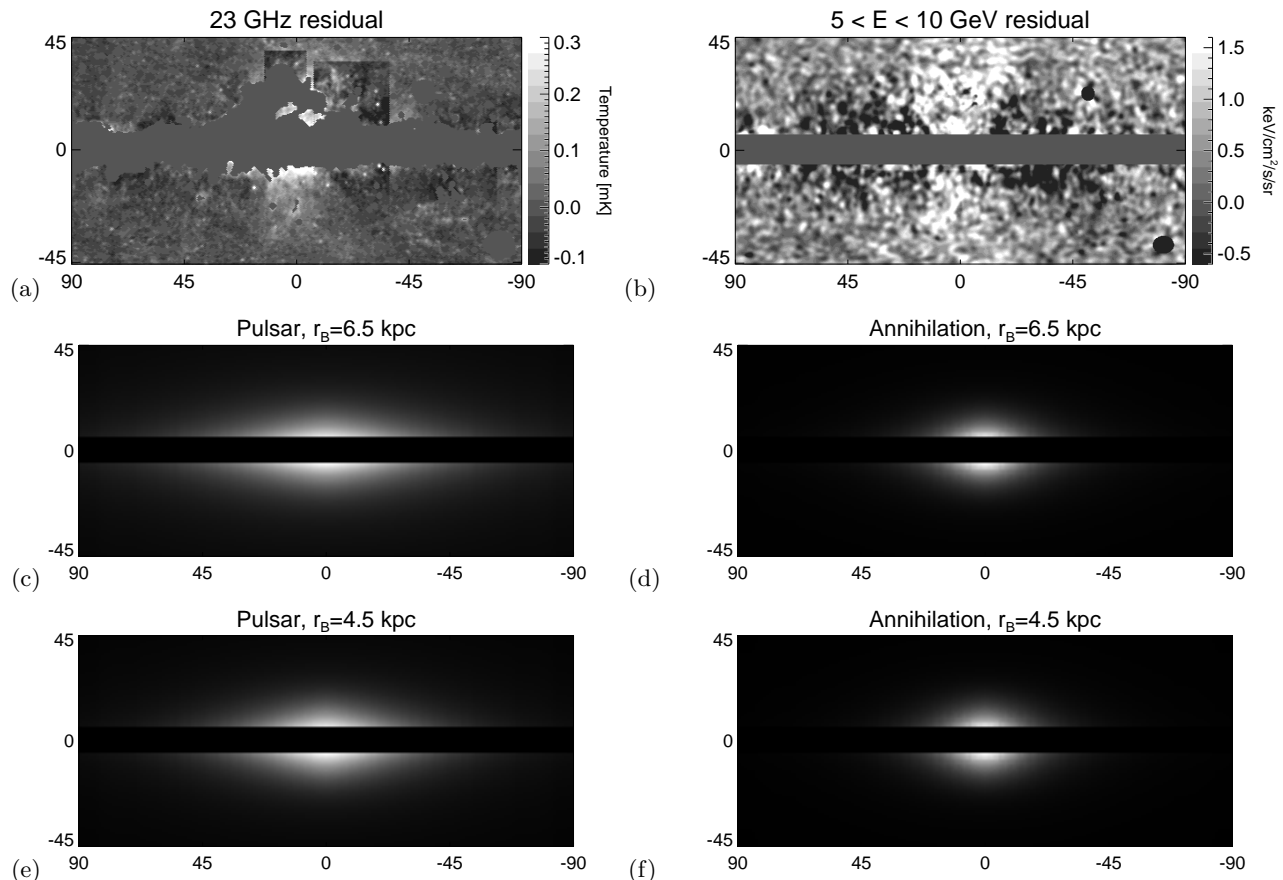


FIG. 1. Maps of the (a) WMAP haze at 23 GHz and (b) Fermi gamma-ray haze at 5-10 GeV for the region $-90 < \ell < 90$ and $-45 < b < 45$. The gamma-ray haze is obtained by subtracting the Fermi diffuse model from the data. All maps are centered on the GC. The data are compared to normalized maps of (c) pulsar synchrotron at 23 GHz and (d) synchrotron at 23 GHz from dark matter annihilation with an Einasto profile. The magnetic field has the form of Eq. 5 with $r_B = 6.5$ kpc. The morphology of the haze signals more closely resembles the signals from dark matter than from pulsars. We show the corresponding results for $r_B = 4.5$ kpc in (e) and (f). Choosing a steeper magnetic field can change the morphology, but this is not preferred by the Haslam data (see Fig. 2). The region $-5 \leq b \leq 5$ is masked out because we only fit the region $b \leq -5$.

is the diffusion coefficient and $b(E, \vec{x})$ is the energy loss rate. This equation holds separately for positrons. For both electrons and positrons, diffusive re-acceleration and galactic convection are negligible above a few GeV. Those effects are often relevant for other cosmic rays, which are governed by similar equations. We use GALPROP v50p.1 to solve for steady state cosmic ray densities. For a review, see [36].

For electrons, the source term includes primary electrons produced by supernovae and secondary electrons produced by collisions of proton cosmic rays on the ISM. We denote these sources by $Q_0(E, \vec{x})$. The source term can also include any new source of electrons, $Q_1(E, \vec{x})$. For positrons, the source term includes only secondary positrons and any new source of positrons. The spectrum of injected secondary e^+e^- is determined by the astrophysics of proton cosmic rays and their interactions.

The injected primary electron spectrum is usually as-

sumed to have the following energy dependence:

$$\frac{dN}{dE} \propto \begin{cases} E^{1.6} & , E < 4 \text{ GeV} \\ E^{\gamma_e} & , 4 \text{ GeV} < E < 2.2 \text{ TeV} \\ E^{3.3} & , E > 2.2 \text{ TeV} \end{cases} \quad (2)$$

where γ_e can vary. dN/dE is the spectrum of e^- per unit source and is continuous. Eq. 2 has often been adopted in the past because the resulting cosmic ray fluxes approximately agreed with the available data. Though we use this form as a default, we will also fit for an arbitrary modification to dN/dE .

The number density for the supernovae that inject these electrons is commonly parametrized as

$$n_s(\vec{x}) \propto r^\alpha \exp\left(-\beta \frac{r}{r_\odot} - \frac{|z|}{.2 \text{ kpc}}\right) \Theta(r_{max} - r) \quad (3)$$

where r is distance to the center of Galaxy, projected on the galactic plane, and z is distance perpendicular to the

galactic plane. The default GALPROP parameters are $\alpha = 2.35$, $\beta = 5.56283$, and $r_{max} = 15$ kpc [37, 38].

The default normalization of the product $n_s \times dN/dE$ is fixed such that the observed local flux from the primary electrons satisfies

$$\frac{c}{4\pi} \frac{dn}{dE}(34.5 \text{ GeV}, z=0, r=r_\odot) = 3.15922 \times 10^{-7} (\text{cm}^2 \cdot \text{sr} \cdot \text{s GeV})^{-1} \quad (4)$$

which is consistent with the flux observed by Fermi.

The diffusion of the injected e^+e^- is governed by the diffusion coefficient, $K(E)$, and L , the escape distance out of the galactic plane. $K(E)$ represents the random walk of a charged particle in tangled magnetic fields, and is approximated as constant in space. It is generally assumed that $K(E) = K_0(E/\text{GeV})^\delta$, where K_0 and δ are propagation parameters. In Table I we give some commonly used values of K_0 , δ , and L . [32, 39]. Our default model assumes $K_0 = 0.097$ kpc²/Myr, $\delta = 0.43$, and $L = 4$ kpc, though we will vary these parameters later. This choice matches cosmic ray data for protons, the B/C cosmic ray ratio, and was used in [40].

As injected electrons and positrons propagate, they lose energy. The energy loss rate $b(E, \vec{x})$ includes energy loss mechanisms. The path length for an electron or positron losing $1/e$ of its energy is typically given by $\sim \sqrt{KE/b}$, which is ~ 1 kpc around 1 GeV and becomes shorter for higher energies, at least until the Klein-Nishina limit [41]. The dominant mechanisms for energy loss are IC scattering and synchrotron, where $b(E) \propto E^2$. Bremsstrahlung (brem), for which $b(E) \propto E$, is subdominant above ~ 1 GeV and is far more localized to the disk. For a new high energy component of e^+e^- , we neglect bremsstrahlung.

The IC rate depends strongly on the model for the interstellar radiation field. We use the default GALPROP model [42] as a baseline. Meanwhile, the synchrotron depends on the model for the magnetic field. We assume a standard parametrization of the field,

$$|B| = B_0 \exp\left(-\frac{r-r_\odot}{r_B}\right) \exp\left(-\frac{|z|}{z_B}\right). \quad (5)$$

r is the distance to the center of the Galaxy, projected on the galactic plane. Typical parameters are $B_0 = 5\mu\text{G}$, $r_B \sim 5-10$ kpc, and $z_B = 2$ kpc.¹ For our default propagation parameters, the GALPROP synchrotron prediction at 408 MHz best matches the Haslam 408 MHz map if $r_B \approx 8.5$ kpc; see Fig. 2.

This parameterization is consistent with observations of the large-scale (ordered) magnetic fields at 1-10 kpc [43]. The random component of the magnetic field is assumed to be proportional to the ordered fields, with a

proportionality factor of approximately one [44]. Thus Eq. 5 is sufficient for our purposes, since our fits are not sensitive to the detailed structure of the magnetic fields. We increase or decrease the average strength of the magnetic fields in the Galactic Center region by decreasing or increasing r_B .

The solution to Eq. 1 is the steady-state cosmic ray density, which then determines the photon signals. The gamma ray flux includes decay of π^0 s produced in proton cosmic ray collisions with the gas in the ISM, IC scattering of e^\pm on interstellar photons, and bremsstrahlung of e^\pm colliding with the ISM. The gamma-ray power in a given direction scales as:

$$P_{\pi^0} \propto \int n_{gas}(s) n_p(s) ds, \quad (6)$$

$$P_{IC} \propto \int n_*(s) n_{e^\pm}(s) ds, \quad (7)$$

$$P_{brem} \propto \int n_{gas}(s) n_{e^\pm}(s) ds. \quad (8)$$

where s is the coordinate along the line of sight. The ~ 23 GHz microwave flux off the Galactic plane is primarily synchrotron radiation of electrons and positrons

$$P_{synch} \propto \int |B(s)|^2 n_{e^\pm}(s) ds \quad (9)$$

where B is the magnetic field.

A new source such as dark matter or pulsars can inject high energy electrons and positrons at 10 GeV to 1 TeV. These new sources are included in $Q_1(E, \vec{x})$. In this paper we solve for the e^+e^- injection spectrum which, after propagation, yields the observed cosmic ray spectrum and gives rise to gamma rays and synchrotron radiation. Our fit will essentially determine $Q_1(E, \vec{x}_0)$, where \vec{x}_0 is the Earth's location. The spatial dependence of Q is fixed to be one of a few conventional models.

These sources can also directly inject photons. There are primary photons from pulsars which are important at lower gamma-ray energies. Given our energy range of interest, we do not consider these further.

In the case of dark matter annihilation or decay, generally there are many channels through which dark matter produces Standard Model particles, which can then decay on short time scales. The end products are e^\pm , neutrinos, and photons. However, we do not consider these direct gamma rays any further. These can be produced from π^0 s, final state radiation² from τ^\pm s or μ^\pm s, or a direct photon channel. For TeV-scale dark matter, these gamma rays can have higher energies than those observed by Fermi. Furthermore, in the fits below it is not difficult to produce enough gamma ray signal above 10-100 GeV. In fact, direct gamma ray production can be rather constrained by observations [45, 46].

¹ The documentation for GALPROP v50p incorrectly states that their parameter B_0 is the magnetic field in the center of the galaxy.

² In some papers, final state radiation is referred to as internal bremsstrahlung. We use ‘‘bremsstrahlung’’ exclusively to mean e^+e^- cosmic rays colliding with the ISM.

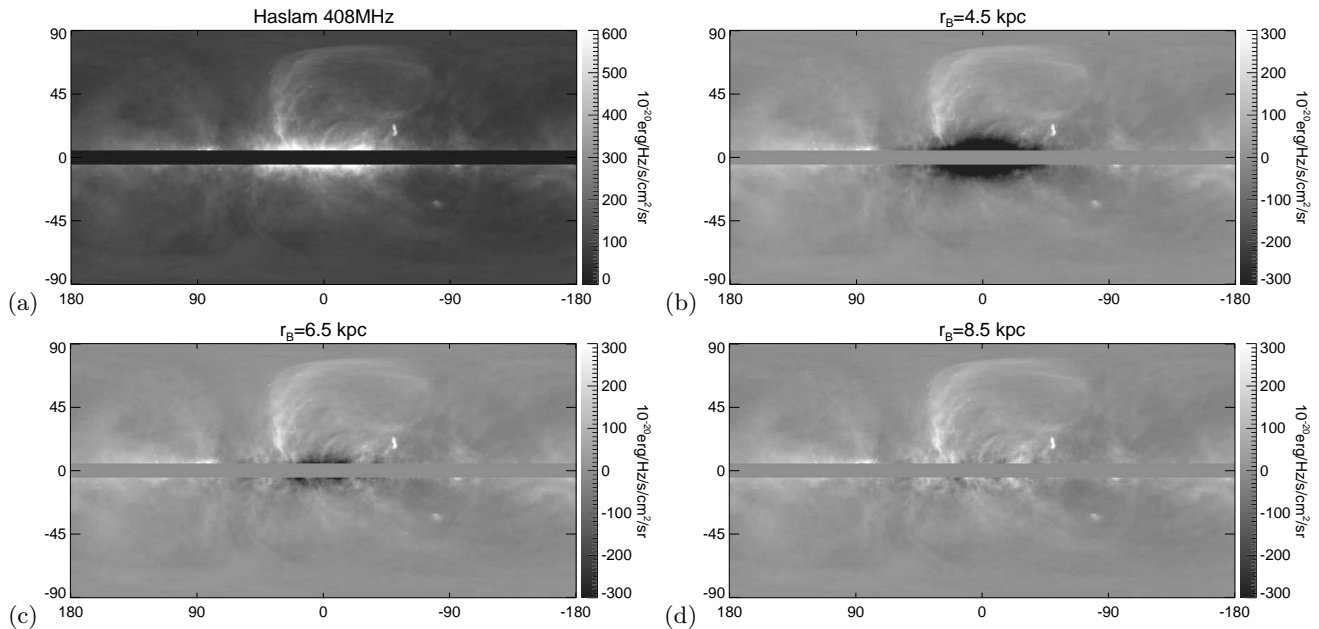


FIG. 2. (a) Haslam 408 MHz map. In the other panels we subtract the default GALPROP model for (b) $r_B = 4.5$ kpc, (c) $r_B = 6.5$ kpc, and (d) $r_B = 8.5$ kpc from the Haslam map. The GALPROP model is normalized such that the total emission in the region $\ell \in [-10, 10], b \in [-90, -5]$ matches the Haslam 408 MHz intensity in the same region. The constant offset is subtracted from the Haslam 408 MHz data. Note that local features like the North polar spur are not modeled in GALPROP and hence are not fit.

A. Data

We fit to the following data:

- PAMELA $J(e^+)/J(e^- + J(e^+))$ positron fraction, which displays a steep rise from 10-100 GeV [5]
- Fermi $(e^+ + e^-)$ cosmic ray spectrum, which shows a slight hardening of the spectrum at a few hundred GeV [1–3]
- Fermi gamma ray spectrum, which shows a hardening of the spectrum at around 10-100 GeV, averaged over the haze region $-15 < \ell < 15$ and $10 < |b| < 30$. Note the pion signal has been subtracted from the data [7]. Our background models match the pion component, shown in Fig. 11 of [7]. This is not affected by the inclusion of new sources of electrons.
- WMAP synchrotron at 23, 33, and 41 GHz averaged over $-10 < \ell < 10$ for $-90 < b < -5$, in 2 degree bins. We also fit to the same data averaged over $10 < |\ell| < 30$, which we call the “high ℓ ” region of the WMAP data and is incorporated to include morphological information from the microwave haze. [6]

These data describe the “anomalous signals”, which suggest the presence of a new source of electrons and positrons, and possibly gamma rays, at roughly 10-1000 GeV.

The Fermi LAT collaboration has provided a reference model for the diffuse emission [47], a detailed fit that includes a reference GALPROP model for IC and models for a number of residual local features giving rise to bremsstrahlung at lower energies. Since we are not studying the detailed structure of the diffuse gamma rays and because IC and pions dominate at high energies, it is sufficient for us to use GALPROP to model the diffuse gamma ray emission in the haze region.

We also do not attempt to fit the Fermi gamma-ray spectrum near the Galactic Center region nor the Fermi isotropic gamma rays. The signal near the GC suffers from large uncertainties in both the dark matter profile and the astrophysical backgrounds. The isotropic signal is extremely sensitive to the halo mass function. Some recent analyses have used these sets of data to constrain dark matter explanations of cosmic-ray signals, for a variety of dark matter models and spatial distributions [45, 46, 48–50]. In Fig. 3 we show that for the best fit spectra and spatial distributions in this paper, there is little or no tension between the predicted total signal and the data in the GC region.

Finally, we also include the following data in order to help regularize the fit at lower energies and higher energies:

- AMS $e^+ + e^-$ cosmic ray spectrum below 10 GeV [51]
- HESS $e^+ + e^-$ cosmic ray spectrum above 900 GeV [52]

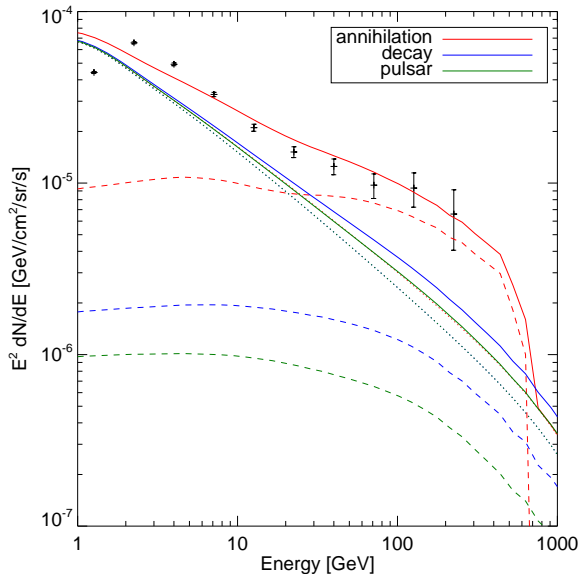


FIG. 3. The fits in this paper are consistent with Fermi observations of the gamma ray spectrum in the region $|\ell| \leq 3$, $|b| \leq 3$. Point sources have been subtracted. Solid colored lines show the predicted total signal for the best fits of the new sources considered in this paper, including backgrounds. The dashed lines show the contribution from only the new source.

Fitting to the data from AMS ensures that the background models are consistent with the low energy cosmic ray data.

We include systematic errors in our analysis and treat them as statistical errors because we do not have the full covariance matrix. The energy calibration error of the Fermi data points is $^{+5\%}_{-10\%}$, but rather than effectively increasing the error bars, we allow for freedom in the normalization of the background, discussed in the next section. The 15% energy calibration error has been included in the error bars used for HESS.

B. Solar Modulation

Though our focus is on high energy data, we ensure that our results are consistent with the low energy (below ~ 10 GeV) cosmic ray data from PAMELA and AMS. However, this data is extremely sensitive to the very local propagation in the heliosphere. To relate the data to GALPROP predictions for the local interstellar (LIS) spectrum outside the heliosphere, it is necessary to apply solar modulation corrections to $e^+ + e^-$ spectra. The solar modulation correction in the force-field approximation is

$$\frac{J_{\odot}(E)}{E^2 - m_e^2} = \frac{J_{LIS}(E + \Phi)}{(E + \Phi)^2 - m_e^2} \quad (10)$$

where Φ is the solar modulation parameter and J is the differential intensity dn/dE [53]. Because of the uncertainty in the force field approximation, we reduce the weight of the PAMELA and AMS data points below 10 GeV, effectively multiplying error bars by a factor of 3. This is adequate to stabilize the fits at low energy.

The solar modulation correction is applied to the GALPROP outputs. We also use the correction when converting the positron fraction data of PAMELA into a positron flux data, using the AMS data on the intensity of $e^+ + e^-$. This will allow the fit to be linear below.

However, these two data sets correspond to different parts of the solar cycle. We thus apply an *inverse* solar modulation correction to the AMS data to obtain the unmodulated positron intensity. Denoting the solar modulation correction by \hat{S}_{Φ} , then the positron signal is obtained from

$$J_{PAM}(e^+) = \left(\frac{J(e^+)}{J(e^-) + J(e^+)} \right)_{PAM} \times \hat{S}_{\Phi_{PAM}^-} \left(\hat{S}_{\Phi_{AMS}^-}^{-1} [J_{AMS}(e^+ + e^-)] \right) \quad (11)$$

where Φ 's are solar modulation parameters. Φ_{PAM}^- is the solar modulation parameter for the PAMELA electrons, which we allow to be different from Φ_{PAM}^+ for the positrons. This approximately captures the charge dependence of the solar physics, visible in the time-dependent positron fraction at lower energies. In the above equation we applied $\hat{S}_{\Phi_{PAM}^-}$ to the total $e^+ + e^-$ signal. Because the positrons are at most $\sim 10\%$ of the total flux, this approximation is justified.

III. FITTING PROCEDURE

We fit for the e^+e^- injection spectrum that, when combined with a background model, best matches the cosmic ray, gamma ray, and microwave observations. The steady-state e^+e^- density is linear in the source function $Q(E, \vec{x})$, so we take a Green's function approach in energy space. The spatial dependence is fixed to be one of a few conventional models in each of the cases below.

We inject delta functions of e^+e^- at various energies and compute the signal from each delta function with GALPROP. Since GALPROP is discretized, in practice this amounts to propagating an appropriately normalized bin of energy. For each of these delta functions, GALPROP computes the steady-state e^+e^- spectrum as well as maps of synchrotron and IC radiation at various energies. We solve for the linear combination of these outputs that best matches the data. The best-fit injection spectrum solution is simply the same linear combination of delta function injections (or in our case, energy bins).

We inject e^+e^- via the source term $Q(E, x)$ in the propagation equation, Eq. 1. For dark matter annihilation, dark matter decay, and pulsars, the new source function $Q_1(E, \vec{x})$ of both positrons and electrons can be

written as

$$Q_1(E, \vec{x}) = \begin{cases} \frac{dN}{dE} \langle \sigma v \rangle_0 BF \frac{\langle \rho_\chi^2 \rangle}{m_\chi^2} \frac{f_E}{2} & , \text{ann} \\ \frac{dN}{dE} \tau_\chi^{-1} \frac{\rho_\chi}{m_\chi} \frac{f_E}{2} & , \text{decay} \\ \frac{dN}{dE} \tau_p^{-1} n_p & , \text{pulsar.} \end{cases} \quad (12)$$

Here dN/dE is the spectrum of electrons or positrons produced per unit source, normalized such that all the power per unit source goes into electrons.³ $\rho_\chi(\vec{x})$ and m_χ are the energy density and mass of the dark matter. $\langle \sigma v \rangle_0$ is the thermal freeze-out cross section for annihilation, $3 \cdot 10^{-26} \text{cm}^3/\text{s}$. BF is a boost factor (from either particle physics or astrophysics such as substructure enhancement). τ_χ is the lifetime in the case of dark matter decay. τ_p and $n_p(\vec{x})$ are rate and density parameters associated with pulsar emission rate and number density. Finally $f_E = f_E(e^+ + e^-)$ is the fraction of energy going to electron-positron pairs. If $f_E = 1$, then the total energy of the electrons will be equal to m_χ for dark matter annihilation and $m_\chi/2$ for dark matter decay.

We also consider arbitrary modifications to the energy dependence of the background primary electron injection, Eq. 2. To accomplish this, we include an extra source of *only* electrons which has the same spatial distribution as the supernovae, Eq. 3:

$$Q_1(E, \vec{x}) = \frac{dN}{dE} \tau_s^{-1} n_s \quad , \text{supernova} \quad (13)$$

where τ_s is an arbitrary rate parameter that is fixed by matching to the data.

Because we do not wish to *a priori* specify model parameters, we instead implement the scenarios above with the following electron injection:

$$Q_1(E, \vec{x}) = \begin{cases} Q_1(E, \vec{x}_0) \left(\frac{\rho_\chi(\vec{x})}{\rho_\chi(\vec{x}_0)} \right)^2 & , \text{ann} \\ Q_1(E, \vec{x}_0) \left(\frac{\rho_\chi(\vec{x})}{\rho_\chi(\vec{x}_0)} \right) & , \text{decay} \\ Q_1(E, \vec{x}_0) \left(\frac{n_p(\vec{x})}{n_p(\vec{x}_0)} \right) & , \text{pulsar} \\ Q_1(E, \vec{x}_0) \left(\frac{n_s(\vec{x})}{n_s(\vec{x}_0)} \right) & , \text{supernova.} \end{cases} \quad (14)$$

where the local injection, $Q_1(E, \vec{x}_0)$ will be determined by the fit (\vec{x}_0 is our location in the galaxy). The positron injection is the same, except in the case of the source injection where there are no positrons injected. Only the spatial profiles distinguish dark matter annihilation, dark matter decay, or pulsars, in our fits.

We bin the energies of the new source, $Q_1(E, \vec{x})$, and treat the particles in each energy bin independently. For example, we generally consider the energy range ~ 5 -5000 GeV with 17 log spaced bins. The propagation of a given injection spectrum is just a linear combination of the propagation of each of the energy bins.

The problem can be treated linearly because high energy e^+e^- are a tiny perturbation to the matter and radiation of the Galaxy. High energy e^+e^- also almost never interact with each other or other cosmic rays; they dominantly interact with the ISM, radiation, and magnetic fields. In GALPROP, the magnetic field is fixed and the usual feedback between cosmic rays and B field is absent. In this limit, the propagation of the individual energy bins is independent.

We use this linearity to invert the propagation problem and determine the injected spectrum $Q_1(E, \vec{x}_0)$, given some assumptions about the spatial density of dark matter or pulsars. Define the vector \mathbf{x} by $x_i = Q_1(E_i, \vec{x}_0)$ for energy bin E_i . The injection everywhere else is determined by the assumed spatial distribution. Also, let b_j be the j th data point minus the galactic background, computed by GALPROP, for that data point.

For each x_i , we propagate the injection and obtain a signal A_{ji} . Thus \mathbf{A} is a matrix which maps \mathbf{x} to the predicted signal, and the columns of \mathbf{A} give the predicted signal from each energy bin. We wish to compare the signal from the new source, $\mathbf{A} \cdot \mathbf{x}$, with the background-subtracted data, \mathbf{b} .

The best fit \mathbf{x} is determined by a goodness-of-fit test, which for a linear problem is a quadratic in the fit parameters:

$$\chi^2 = (\mathbf{A} \cdot \mathbf{x} - \mathbf{b})^T \mathbf{C}^{-1} (\mathbf{A} \cdot \mathbf{x} - \mathbf{b}) \quad (15)$$

where \mathbf{C} is a covariance matrix containing the errors on the data. This is just a quadratic minimization problem. Note that we also include several other parameters in \mathbf{x} that allows us to slightly modify the background predictions and improve the fit. This is described further in the following subsection.

Finally, it is possible to obtain dN/dE and the other parameters in Eq. 12. This will be possible for the dark matter scenarios with additional constraints on $\int E dN/dE dE$ and where dN/dE cuts off. This is discussed more below when we describe the results for the scenarios above.

A. Uncertainties

The predictions for the signals discussed in this paper can have significant theoretical and astrophysical uncertainty. To capture the effects of these uncertainties, we include several parameters in the fits that essentially allow for (small) variations in the background model.

The main uncertainties are in the background primary and secondary e^+e^- injection, since we are fitting all the data that could possibly constrain this. (For a more detailed discussion of uncertainties in the cosmic rays signals, see [54, 55].)

In the primary injection, we allow γ_e in Eq. 2 to vary in discrete steps. We also fit for an arbitrary normalization factor N_p relative to the condition in Eq. 4. Usually we find $N_p \approx 1.0$ because the condition was chosen to

³ The specific condition can be found in Sec. IV A for dark matter annihilation and Sec. IV B for dark matter decay.

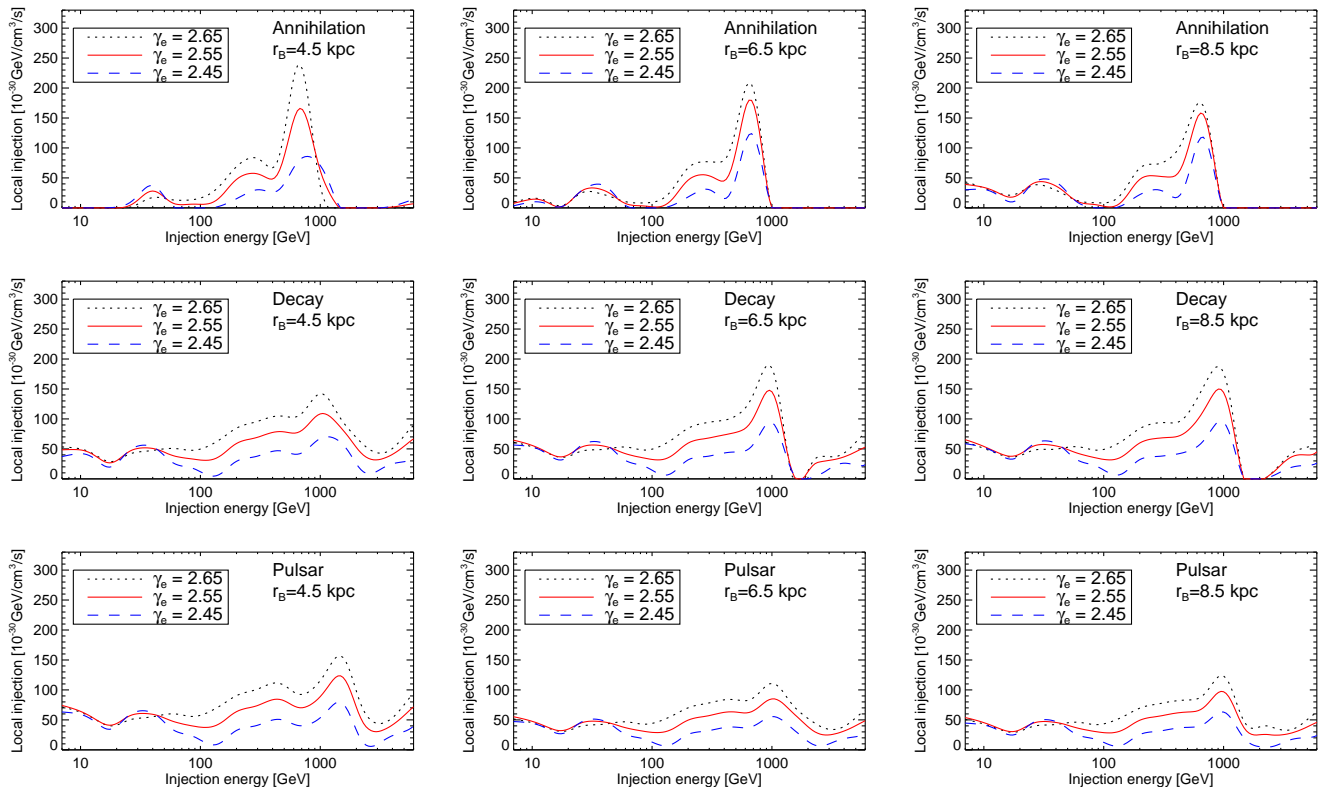


FIG. 4. All fit results for the three scenarios, over a 3×3 grid in background electron injection index ($\gamma_e = 2.45, 2.55, 2.65$) and scale for the magnetic field $r_B = 4.5, 6.5, \text{ and } 8.5$ kpc. These spectra were obtained from non-negative fits; the interpolated local injection density is plotted. Despite a wide range of assumptions about the background model, the results remain the same, qualitatively, for each scenario.

approximately match the Fermi cosmic ray data. The source spatial distribution for primary electrons, Eq. 3, is also uncertain. Rather than considering the full range of possible source distributions, we simply allow for a different normalization factor of the primary electron spectrum near the Galactic Center, relative to Eq. 4. Because the diffusion length is ~ 1 kpc, this will not affect the local cosmic ray signal. This normalization factor, N_h , is fixed by matching the synchrotron background prediction onto the Haslam 408 MHz synchrotron map [56] for $-90 < b < -5$, averaged over $-10 < \ell < 10$. The contribution from the new high-energy source is negligible at this frequency.

As for the secondary e^+e^- , it was shown in [32] that modifying the propagation parameters effectively changes the overall normalization of the local steady-state secondary positron flux by up to an order of magnitude. Thus rather than scanning over a large set of propagation parameters consistent with all the low energy cosmic ray data, we allow the normalization of the secondaries to be a fit parameter, N_s .⁴

There are several other adjustable parameters that can improve the fit and allow for variations in the background model. We give the complete list below. None of these will change the predictions for other cosmic ray data.

The following parameters characterize the uncertainties of our theoretical models. We fit for these parameters simultaneously with the injection spectrum, as their effects can also be treated linearly:

- N_{IC} : The normalization of the background IC signal near the center of the galaxy, relative to the GALPROP prediction. There are many uncertainties in the starlight density and spatial variations in the primary electron density near the galactic center.
- ΔS : Zero-points of the WMAP signal. We allow a different one for each data set.
- N_s : Normalization of secondary local electron spectrum, relative to the GALPROP output for our

⁴ We show the effect of changing propagation parameters on some

fits in Fig. 5. The result does not differ significantly relative to the error bars.

choice of propagation parameters. This can vary by up to an order of magnitude given theoretical uncertainties [55, 57].

- N_p : Normalization of **local** primary electron spectrum, relative to Eq. 2. As mentioned above, this factor does not have to be the same as N_h .

We include these parameters in \mathbf{x} , and \mathbf{A} is enlarged to include extra columns corresponding to each of these background signals.

The signals are not linear in the following parameters, so we scan over a discrete set of these:

- r_B : The r -scale of the galactic B field, where the local B field is fixed to $5 \mu G$. See Eq. 5. We include $r_B = 4.5, 6.5,$ and 8.5 kpc, corresponding to $B = 33, 18,$ and $14 \mu G$ in the center of the Galaxy. We used $z_B = 2$ kpc.
- γ_e : The index of the primary electron injection spectrum above 4 GeV. We include $\gamma_e = 2.45, 2.50, 2.55, 2.60, 2.65,$ and 2.70 .
- $\Phi_{AMS}, \Phi_{PAM}^+, \Phi_{PAM}^-$: Solar modulation parameters for AMS and PAMELA, in the force-field approximation, as described in Section II B.

Though we allow these to be fit parameters, clearly in reality they have some definite form independent of our model. In Fig. 4 we show the best fit for a grid in r_B and γ_e . Though the spectra do change, the qualitative features remain roughly the same.

B. χ^2 minimization and regularization

We are minimizing

$$\chi^2 = (\mathbf{A} \cdot \mathbf{x} - \mathbf{b})^T \mathbf{C}^{-1} (\mathbf{A} \cdot \mathbf{x} - \mathbf{b}) \quad (16)$$

where \mathbf{x} is a vector of parameters we fit for, containing the injection spectrum as well as the normalization parameters and offsets described above. \mathbf{C} is a covariance matrix, so it is symmetric and positive. It can then be shown that the matrix $\mathbf{A}^T \mathbf{C}^{-1} \mathbf{A}$ is positive semi-definite.

Ideally the spectrum we derive is smooth and non-negative. However, the existence of null (or nearly null) eigenvalues of $\mathbf{A}^T \mathbf{C}^{-1} \mathbf{A}$ means that there are directions in the parameter space where we can modify the spectrum by large values with little change to the observed signals. This corresponds to, for example, changing the spectrum for two neighboring energy bins by a large positive and negative amount respectively, such that the observed signal remains nearly the same.

We regularize the spectrum by using only 17 log-spaced bins between 5 GeV and 5000 GeV. We also perform a non-negative quadratic fit following the algorithm in [58]. All of the fit parameters should be positive except for ΔI which we find is always of the same sign for our data, so we can choose a convention where it is positive.

To obtain errors on the spectrum, we find the eigenvectors and eigenvalues of $\mathbf{A}^T \mathbf{C}^{-1} \mathbf{A}$. This allows us to change basis from the parameter space in \mathbf{x} to a new parameter space \mathbf{y} where χ^2 is separately parabolic in each parameter. The variance of these new parameters \mathbf{y} is determined by computing the allowed shift of each parameter, relative to the best fit, such that $\Delta\chi^2 = \pm 1$. Even though a non-negative constraint was imposed for the best fit, we consider the entire space of solutions within $\Delta\chi^2 = \pm 1$.

Each x_i is a linear combination of the y_i , so we sum the squares of the contribution from each y_i to find the variance in x_i . The quoted error on each x_i is the square root of the variance. Because we are performing a non-negative fit, however, the positive and negative errors can be different.

In Fig. 5 we show the entire range of possible variations of the best fit injection spectrum with $\Delta\chi^2 = \pm 1$. We add to the best-fit spectrum all possible variations along the eigendirections, or all independent variations of y_i . (We do not show the background normalization coefficients and WMAP offsets, though they are simultaneously varying with the injection spectrum.)

We also considered several alternative methods of regularization, rather than non-negativity. As an example, we can impose smoothness by adding terms to χ^2 :

$$\chi_{eff}^2 = \chi^2 + \eta_1 (\mathbf{D}_E \cdot \mathbf{x})^T \cdot (\mathbf{D}_E \cdot \mathbf{x}) + \eta_2 (\mathbf{D}_E^2 \cdot \mathbf{x})^T \cdot (\mathbf{D}_E^2 \cdot \mathbf{x}) \quad (17)$$

where \mathbf{D}_E and \mathbf{D}_E^2 are finite difference and second-difference matrices, respectively. These matrices *only* act on the injection spectrum and not the other fit parameters such as normalization factors and WMAP offsets. η_1 and η_2 are tunable parameters that control the smoothness of the fit. In Fig. 5 we show the best fit using this regulator instead of the non-negative regulator above. For an appropriate range of η_1 and η_2 the solution is qualitatively similar to the non-negative result. Similarly, we tested several other regulation techniques, such as suppressing variations in nearly null eigendirections. Again, for “reasonable” regulators, the result is qualitatively similar.

IV. RESULTS

We determined the best-fit injection spectrum for 350 data points from Fermi, PAMELA, WMAP, AMS, and HESS. There are 29 fit parameters coming from 17 energy bins, 3 normalization factors, 6 WMAP offsets, and 3 solar modulation parameters. Including r_B and γ_e , then there are 31 fit parameters. Our results are summarized in Table II and in Figs. 7-10. The details of the fit results for each scenario can be found in the following sections.

In each of the following figures, we show the fits to the

- e^+e^- flux data from Fermi, AMS, and HESS

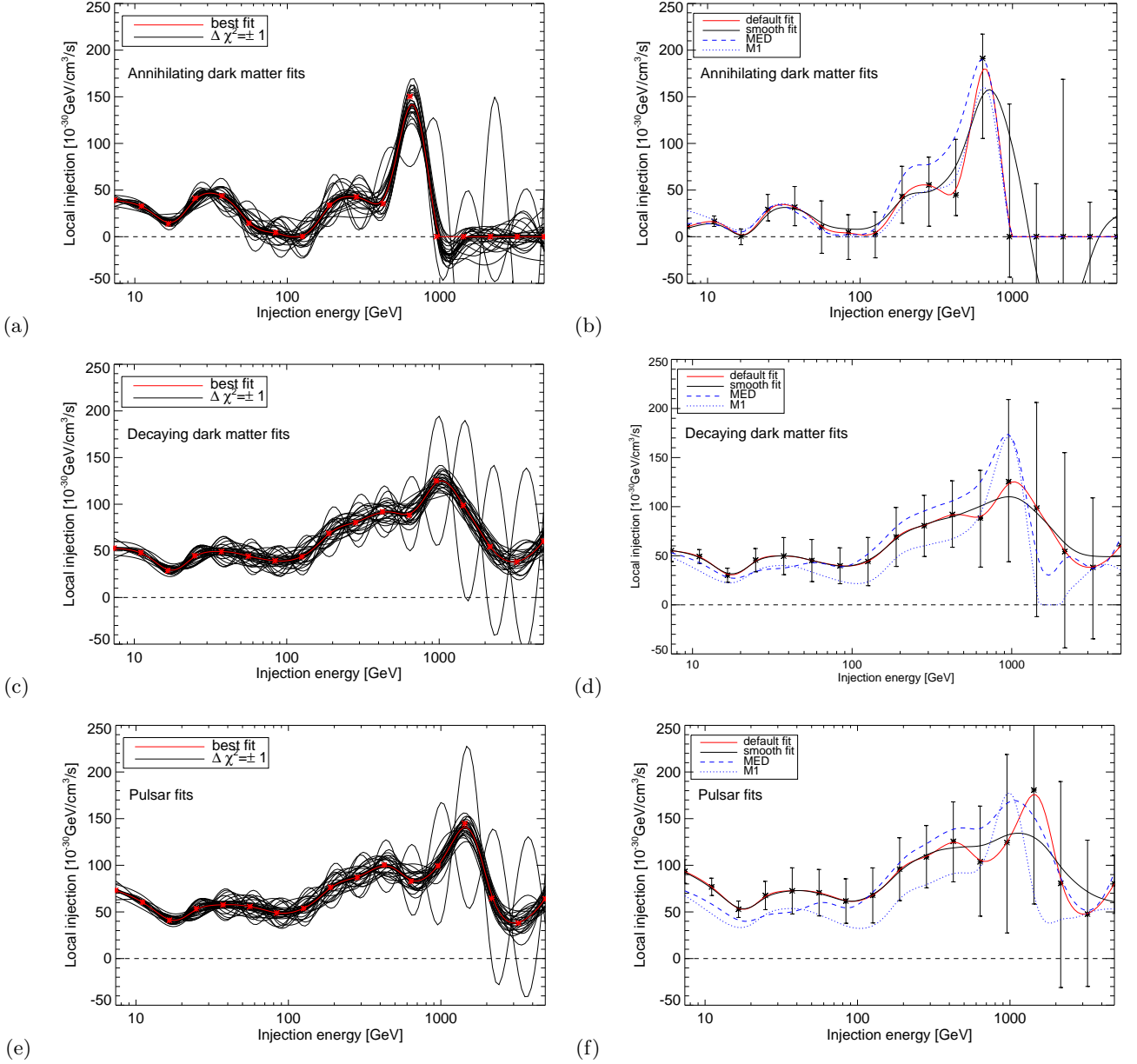


FIG. 5. In the left column we show the space of possible solutions within $\Delta\chi^2 = \pm 1$ of the best-fit solution, which was obtained from a non-negative fit. The red lines are the best fits for (a) dark matter annihilation, (c) dark matter decay, and (e) pulsars. The spectra shown are interpolated between the bins (marked by red stars). In the right column we show other best fits obtained from using different propagation parameters, given in Table I, or a different fitting regulator that enforces smoothness of the solution (from Eq. 17). Our results are robust to very different propagation parameters. The fit for M2 is not shown because L is only 1 kpc. Since the haze signals extend out to ~ 4 kpc or more, it is impossible for this set of propagation parameters to produce the haze.

- positron flux obtained from combining the AMS and PAMELA data in Eq. 11
- positron flux fraction $J(e^+)/J(e^- + J(e^+))$ from PAMELA for comparison, though we did not directly fit to this data
- WMAP synchrotron data at 23 GHz and 33 GHz,

and 23 GHz at high ℓ ; the data for 41 GHz and the high ℓ data for 33 GHz and 41 GHz are included in the fit, but not shown because the fit looks extremely similar to the plots already shown

- Haslam 408 MHz data, used to fix N_h , as discussed in Sec. III A

	SN	Ann1	Ann2	Decay	Pulsars	Ann+Pulsar	Ann+SN
Figure	6	7		8	9	10	11
Einasto α		0.22	0.22	0.12		0.17 [†]	0.17 [†]
γ_e	2.65	2.5	2.5	2.6	2.6	2.55	2.55
r_B [kpc]	8.5	8.5	6.5	4.5	4.5	6.5	8.5
Φ_{AMS} [GeV]	0.52	0.42	0.46	0.46	0.42	0.48	0.48
Φ_{PAM}^+ [GeV]	0.08	0.20	0.18	0.04	0.02	0.12	0.18
Φ_{PAM}^- [GeV]	0.0	0.3	0.1	0.3	0.3	0.3	0.1
N_{IC}	1.8	1.3	1.6	2.5	2.6	1.3	1.2
N_s	1.8	0.9	1.4	0.6	0.5	0.9	1.6
N_p	1.0	1.1	1.1	1.0	1.0	1.0	0.9
χ^2	30*	139	144	129	148	111	111
χ_{red}^2	.51	.44	.45	.41	.46	.37	.37
m_χ [GeV]		1000	1000	$\gtrsim 16000$		300	300
$BF \times f_E$		70	70			10	10
τ_χ/f_E [s]				$< 10^{26}$			

TABLE II. Best fit parameters for annihilating dark matter, decaying dark matter, and pulsar cases to 350 data points. Ann1 and Ann2 had nearly the same χ^2 but had different r_B so both results are displayed. In the supernova (SN) injection case there were 91 data points. We obtained mass, boost factor, and lifetime parameters from the best fit. In the last two columns we show fit results for linear combinations of these three scenarios. The fit errors on the normalization parameters N are less than 5-10% and thus are not shown. [†]For the combination cases, we fixed the dark matter profiles to have Einasto $\alpha = 0.17$.

- Fermi gamma ray data, where the π^0 background has been subtracted [7]

along with the best-fit local injection, $E^2 Q_1(E, \vec{x}_0)$.

Before discussing the fits in detail, we emphasize that the results in Table II and the spectra plotted here are not meant to be taken as precise answers but as qualitative guidelines for the necessary spectra, for each scenario, in order to explain the data. As shown in Fig. 4, the spectra vary with the background model, but the general features remain the same. Errors and variations in the solution were discussed in Section III B. In addition, the effect of changing propagation parameters is shown in Fig. 5.

Specific bumps and features in the spectra we find are more likely signs that the smooth background models we have assumed are not adequate. If there is any large systematic or unmodeled effect in the Fermi cosmic ray data, for example, it can change the features in best fit spectrum significantly. In particular, note that the shape of the high energy region of each spectrum above ~ 100 GeV is only constrained by the high energy Fermi cosmic ray data since the Fermi gamma ray data is primarily only sensitive to the total power in this energy range. The other data are almost completely insensitive to such high energy particles. Thus the error bars on these bins are typically the largest. Furthermore, the high energy spectrum is more sensitive to changes in γ_e (see Fig. 4).

The low energy part of the spectrum is more severely constrained by all of the data. However, the low energy spectrum is also extremely sensitive to the bumps and features in the Fermi cosmic ray spectrum at low energies. This is very likely a sign that some features in the Fermi

cosmic ray spectrum have not been properly included in the background model. For example, in Fig. 11 we show a fit which allows both dark matter annihilation and an arbitrary modification to the energy dependence of the supernovae-injected electrons. The low-energy features can be fit by a modification of the supernova electron spectrum, while dark matter annihilation is still necessary to explain the signals above 10-20 GeV.

Fig. 6 shows the “supernova” fit of the low energy PAMELA data, all of the e^+e^- data, and the gamma ray data to a disk-like source with only electrons. This corresponds to a modification of the background primary electron spectrum and is implemented using the injection in Eq. 14. The best fit spectrum we found is a hardening of the injection up to 1 TeV. Though this source modification can easily match the cosmic ray or IC data, the disk-like spatial profile and lack of positrons produced are starkly inconsistent with the synchrotron signal and the PAMELA data. A new source is required.

A. Annihilating Dark Matter Results

The form of the injection for annihilating dark matter was given in Eq. 14 and Eq. 12. We assume the local dark matter density is $\rho_0 = 0.4 \text{ GeV}/\text{cm}^3$ [59].

Conventionally used dark matter halo density profiles are obtained by simulations and can be approximated by an Einasto profile, with $0.12 \lesssim \alpha \lesssim 0.22$ and $\alpha \approx 0.17$ on average [60]. This does not include substructure effects which can modify the effective spatial profile used

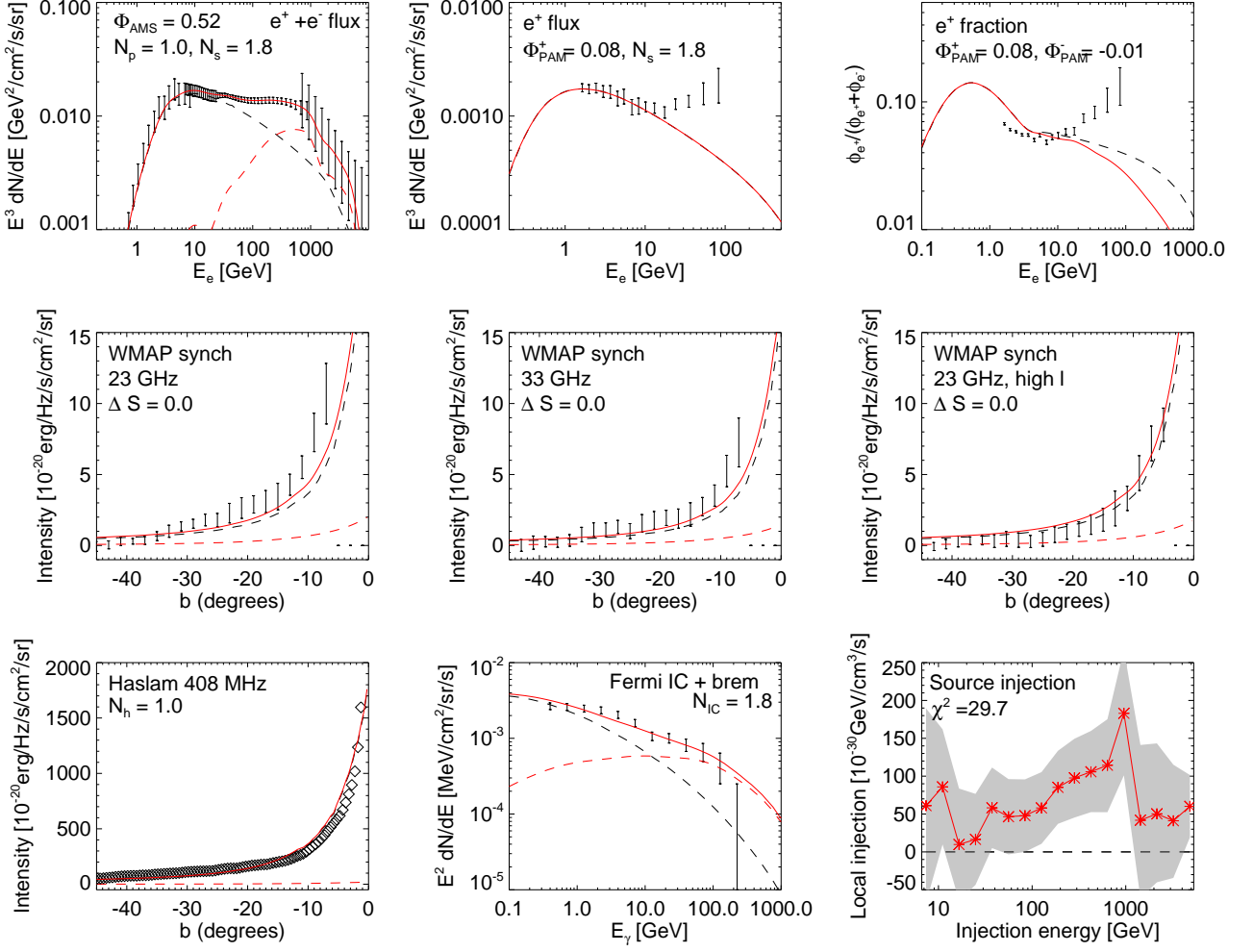


FIG. 6. Best fit to a modification of the primary electron injection spectrum, with $\chi^2_{red} \approx .51$. Black dashed lines are the background prediction for a model with $\gamma_e = 2.65$ and $r_B = 8.5$ kpc, though in this case we are fitting for the true background. Red dashed lines give the contribution of the new source injection, and solid red lines are the total. The gray shaded region is the error estimate on the best-fit injection spectrum. We have not attempted to fit the PAMELA data or the WMAP haze, which are difficult to produce.

in Eq. 12, as in [61].

We allow values of $\alpha = 0.12, 0.17$, and 0.22 , with a core radius of $r_{-2} = 25$ kpc. In practice the shallower profile with $\alpha = 0.22$ is always the best fit to avoid over-producing the gamma ray signal. These profiles only differ by a factor of ~ 2 at .1 kpc from the center of the galaxy. Though NFW profiles are also commonly used, their signatures can be approximated by one of these Einasto profile. We also considered spatial profiles which were Einasto squared times an $r^{1/4}$ or $r^{1/2}$ scaling, corresponding to an r dependent cross section [62]. Using these profiles can improve the χ^2 by 5-10, but the injection spectrum does not change significantly.

In the annihilating case we found best fits with magnetic fields of $r_B = 4.5, 6.5$, and 8.5 kpc, all with χ^2 around 140 and $\chi^2_{red} \approx .44$. Conventional magnetic

field models have r_B closer to 8.5 kpc. Furthermore, in this case, the normalization factors N are ~ 1 , so that the model is self-consistent. Thus we show the fit with $r_B = 8.5$ kpc in Fig. 7. In Table II we give the fit parameters for $r_B = 6.5$ kpc under the column “Ann2”.

For all three magnetic fields above, we found that an injection index of $\gamma_e = 2.5$ for the primary electron signal optimized the ratio between the PAMELA and the Fermi $e^+ + e^-$ apparent dark matter components. However, for $r_B = 8.5$ kpc the fit does not match the PAMELA data as well, as an excess of cosmic rays above 100 GeV can produce too many gamma rays through IC scattering.

We can estimate several model parameters from the best-fit spectrum by relating Eq. 14 and Eq. 12. To find the dark matter mass, we assume dN/dE cuts off at around m_χ . Though this estimate of m_χ depends on the

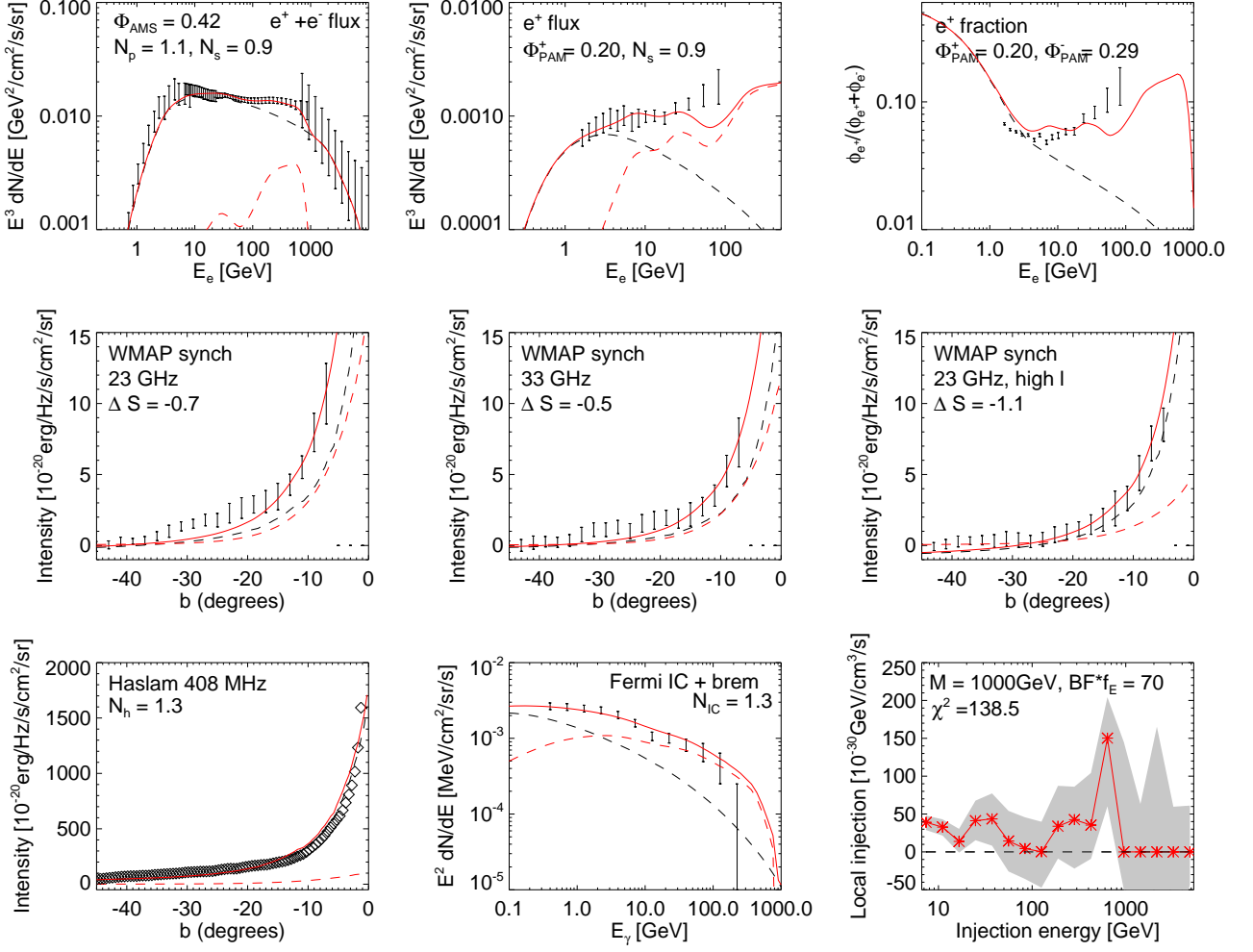


FIG. 7. Best fit for the annihilating dark matter scenario, with $\chi_{red}^2 \approx .44$. The spatial profile of the dark matter is Einasto with $\alpha = 0.22$. Black dashed lines are the background prediction for a model with $\gamma_e = 2.5$ and $r_B = 8.5$ kpc. Red dashed lines give the contribution of the new source injection, and solid red lines are the total. The gray shaded region is the error estimate on the best-fit injection spectrum.

rather uncertain high-energy part of the injection spectrum, values of roughly 1 TeV are expected given the turnover in the $e^+ + e^-$ data around 600-1000 GeV and the turnover in the gamma-ray spectrum at 100-200 GeV.

Next, dN/dE was defined such that the total energy of the emitted particles sums to the mass of dark matter:

$$\int E \frac{dN}{dE} dE = m_\chi. \quad (18)$$

Therefore, integrating the local injection multiplied by energy gives

$$\int E Q_1(E, \vec{x}_0) dE = \langle \sigma v \rangle_0 BF \frac{(\rho_0)^2}{m_\chi} \frac{f_E(e^+ + e^-)}{2}. \quad (19)$$

Given an estimate of m_χ , we can therefore estimate $BF \times f_E(e^+ + e^-)$ in terms of the best fit local injection and known parameters.

B. Decaying Dark Matter Results

For the decaying dark matter case, we assume the same range of dark matter density profiles as in the annihilating case. Again, in practice we will be limited to the case where $\alpha = 0.12$. This time a steeper profile is required to produce sufficient synchrotron signal to fit the WMAP data.

The model parameters can be determined from Eq. 12 and Eq. 14. We assume dN/dE cuts off at around $m_\chi/2$ this time. Again, this cutoff is rather sensitive to the high-energy part of the spectrum, which has large error

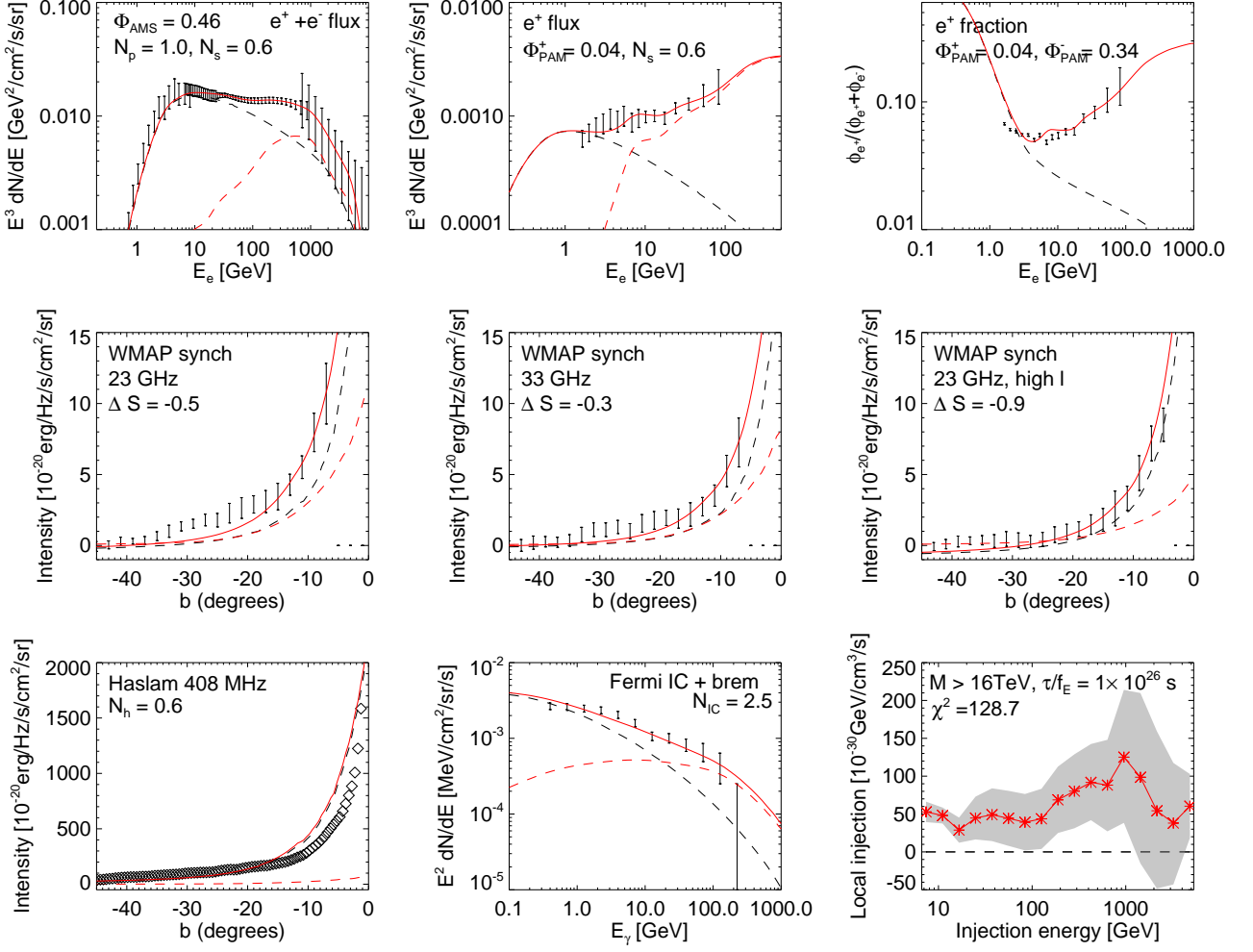


FIG. 8. Best fit for the decaying dark matter scenario, with $\chi^2_{red} \approx .41$. The spatial profile of the dark matter is Einasto with $\alpha = 0.12$. Black dashed lines are the background prediction for a model with $\gamma_e = 2.6$ and $r_B = 4.5$ kpc. Red dashed lines give the contribution of the new source injection, and solid red lines are the total. The gray shaded region is the error estimate on the best-fit injection spectrum.

bars, but values of $\gtrsim 2$ TeV are expected given the data.

By definition, dN/dE satisfies

$$\int E \frac{dN}{dE} dE = m_\chi/2. \quad (20)$$

Again, we integrate the local injection multiplied by energy, giving

$$\int E Q_1(E, \vec{x}_0) dE = \tau_\chi^{-1} \frac{\rho_0}{2} \frac{f_E(e^+ + e^-)}{2}. \quad (21)$$

This allows us to determine the dark matter lifetime over the energy fraction. However, note that in many cases, dN/dE does not cut off in the energy ranges we consider and the spectrum is essentially unconstrained at higher energies. Then we only obtain bounds on the mass and lifetime.

The best fit is shown in Fig. 8. There is no clear mass cutoff in the best-fit spectrum, so the mass of the particle can be from ~ 4 TeV to greater than 16 TeV.

Because in the decaying scenario the injected power is proportional to ρ_χ and not ρ_χ^2 , generally it is harder to generate enough synchrotron and IC signal. Both of these signals are in regions at least 5 degrees off of the galactic plane. The steeper dark matter profile with $\alpha = 0.12$ is not enough to produce the signals.

We found $r_B = 4.5$ kpc can increase synchrotron near the center of the galaxy, but this gives a somewhat unconventionally high value of the magnetic field in the GC, $33\mu G$. Fig. 2 shows that $r_B = 4.5$ kpc also gives the poorest fit to the Haslam data, especially compared to $r_B = 8.5$ kpc. In addition, a somewhat large injection of low energy electrons and positrons is required. However, for this large magnetic field, the IC signal drops. Thus

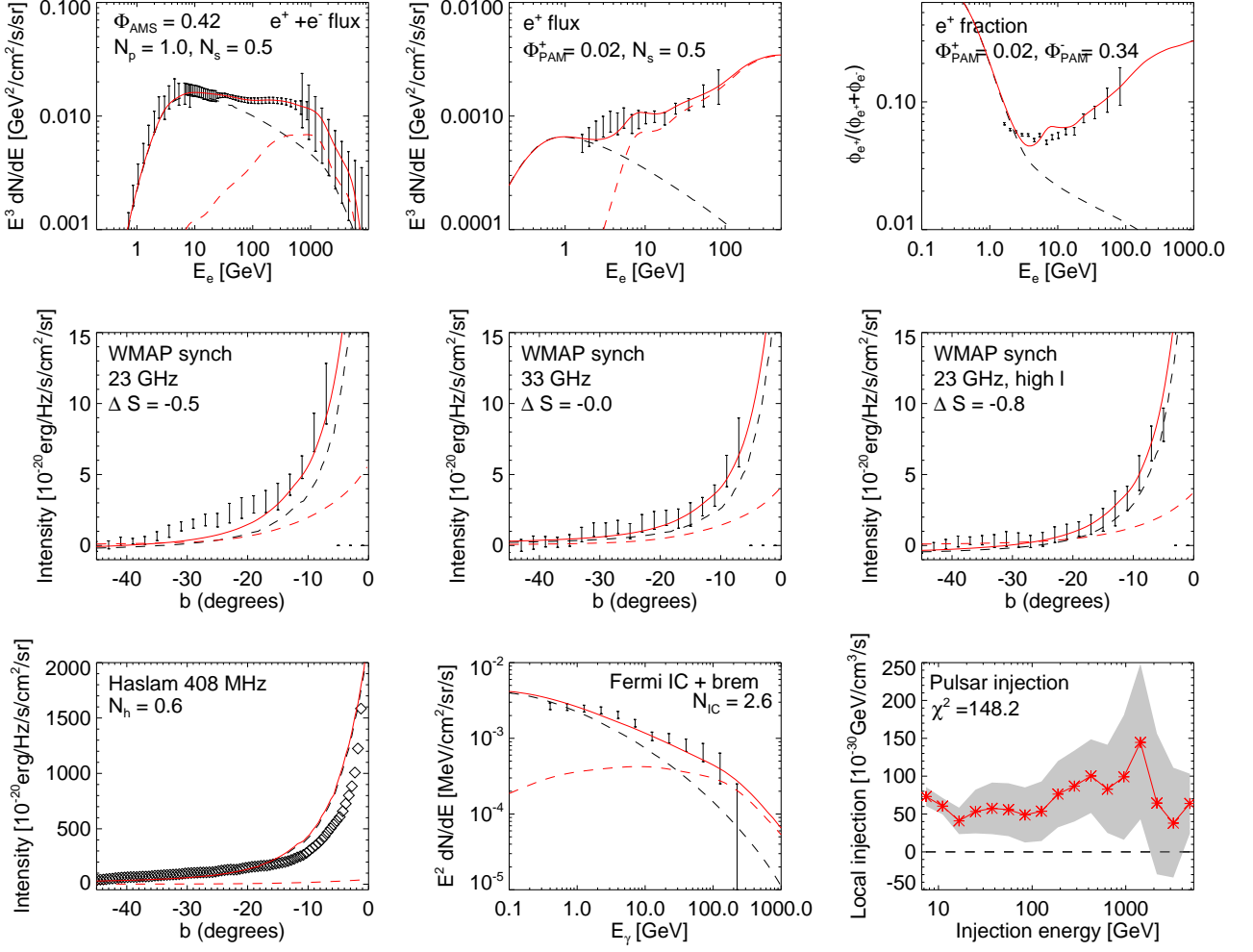


FIG. 9. Best fit for the pulsar scenario, with $\chi_{red}^2 \approx .46$. The pulsar profile is given by Eq. 22. Black dashed lines are the background prediction for a model with $\gamma_e = 2.6$ and $r_B = 4.5$ kpc. Red dashed lines give the contribution of the new source injection, and solid red lines are the total. The gray shaded region is the error estimate on the best-fit injection spectrum.

the normalization N_{IC} is rather large, $N_{IC} \sim 2.4$. Even for fits with $r_B = 6.5$ kpc, it was necessary for $N_{IC} \sim 2$ to obtain sufficient IC signal. This corresponds to rather high starlight density.

While it is possible that the decaying dark matter can also produce gamma rays directly or through FSR, these signals are typically at higher energies, above 10-100 GeV. In this case, the large N_{IC} factor for the background IC signal indicates that there is a depletion of gamma rays at low energies, below 10 GeV.

Though the decaying scenario nominally gives the best $\chi^2 \approx 130$ and $\chi_{red}^2 \approx .41$, the large normalization factors demand a more self-consistent modeling of backgrounds and uncertainties in order to fully justify the goodness of fit.

C. Pulsar Results

The range of types of pulsars, their spatial distributions, and their e^+e^- spectra is not well determined. As a crude model, we posit some spatial profile for the number density of pulsars and assume the spectrum of electrons and positrons has the same energy dependence everywhere. Generally pulsars are concentrated in the galactic disk, making it difficult to produce the haze. In Fig. 1 we compare the morphology of the synchrotron haze produced by pulsars to that produced by dark matter. It is possible, however, that certain types of pulsars have a more spherical distribution [63].

We consider the following range of pulsar profiles, which span those typically used in the literature. (See [30, 64] for examples and references.) Assume a density

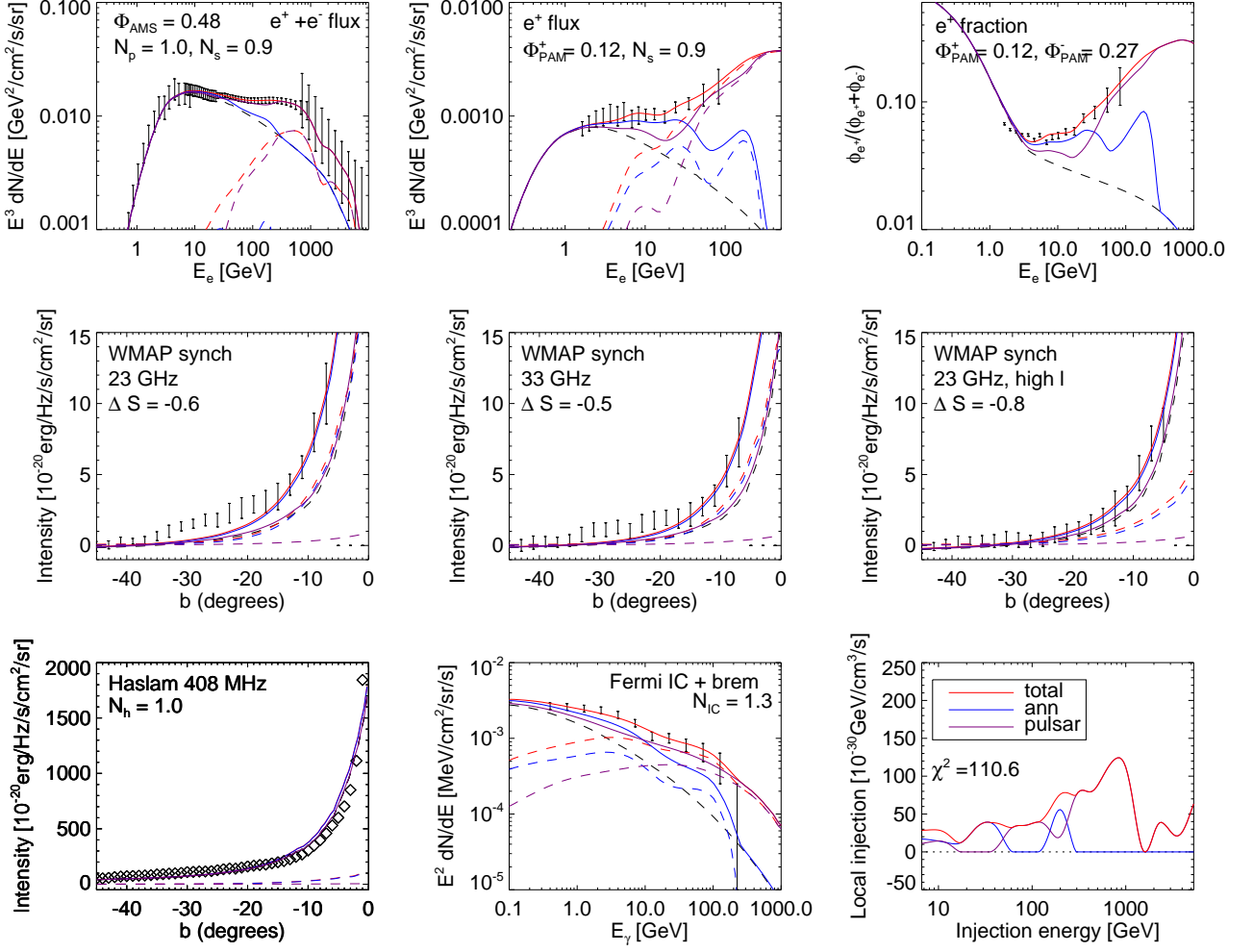


FIG. 10. Best fit for a linear combination of annihilating dark matter and pulsars, with $\chi^2_{red} \approx .37$. The dark matter spatial profile is Einasto with $\alpha = 0.17$. Black dashed lines are the background prediction for a model with $\gamma_e = 2.65$ and $r_B = 8.5$ kpc. Colored dashed lines give the contributions from new sources, while colored solid lines give the total signal from new source and background.

profile of the form

$$n_p \propto \exp\left(-\frac{|z|}{z_p}\right) n_\rho(\rho) \quad (22)$$

where $\rho = \sqrt{x^2 + y^2}$ and the origin is at the center of the galaxy. We include profiles with $z_p = 0.08, 0.5$, and 2 kpc. For the radial profile,

$$n_\rho \propto \exp\left(-\frac{\rho}{4.5 \text{ kpc}}\right). \quad (23)$$

In practice, the three cases above look nearly identical because of diffusion. Another commonly used profile has $n_\rho \sim \rho \exp(-\rho/4.0 \text{ kpc})$. However we do not consider this option further because the suppressed density near the center of the galaxy makes it even more difficult to produce the haze.

Qualitatively, the pulsar results, Fig. 9, are rather similar to the decaying dark matter results, though the fits are even worse because of the disk-like rather than spherical profile. The best fit has $r_B = 4.5$ kpc with significant low-energy injection and large normalization factor N_{IC} of 2.6. Though it is possible that pulsars can produce many low-energy gamma rays, it is unlikely these gamma rays can compensate for the background gamma-ray signal being 2 – 3 times too low. For $r_B = 6.5$ kpc or 8.5 kpc, the pulsar scenario cannot produce sufficient synchrotron signal.

D. Combination Results

We fit for linear combinations of annihilation, decay, pulsars, and supernova injections, which not surprisingly

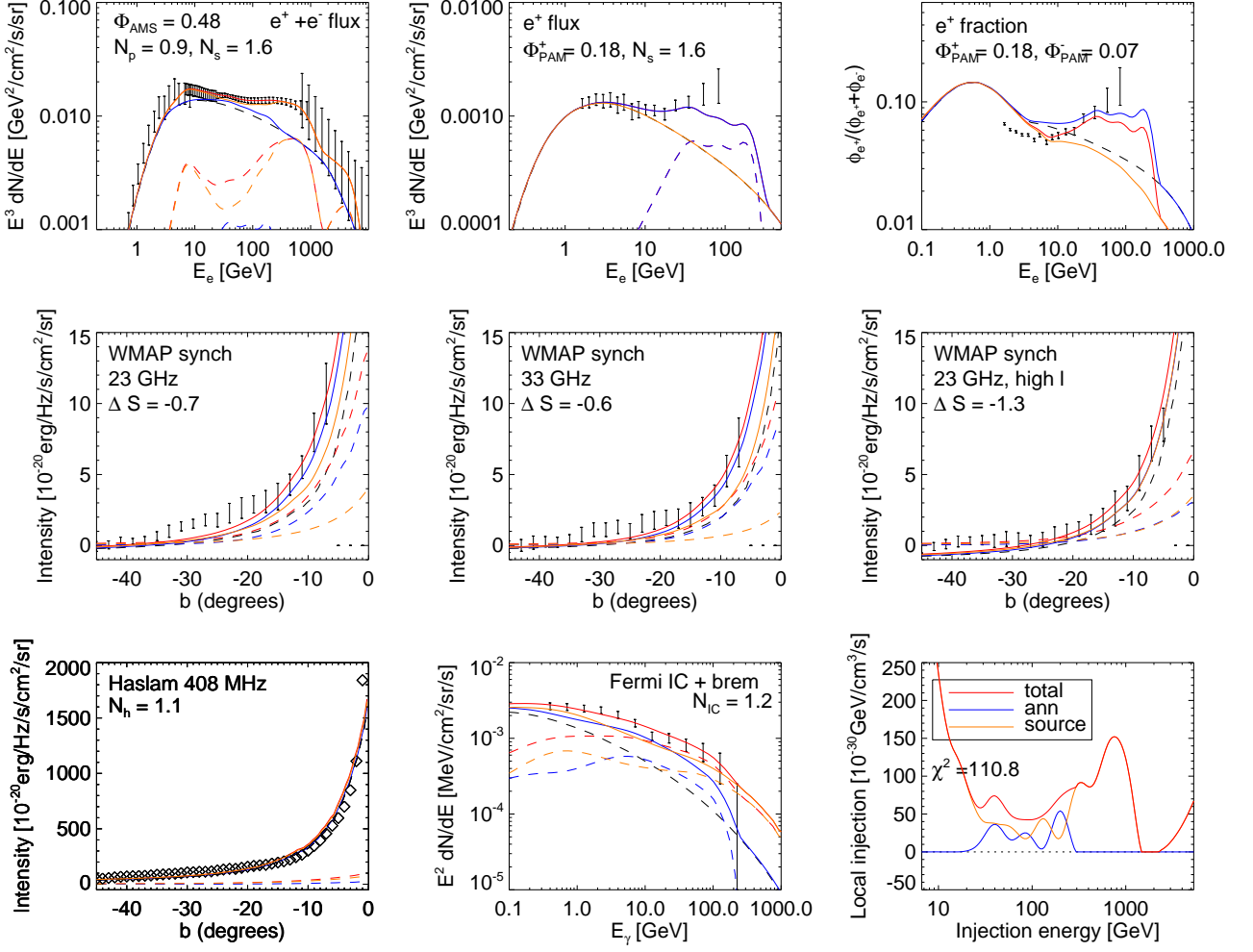


FIG. 11. Best fit for a linear combination of annihilating dark matter and an arbitrary modification to the primary electron injection spectrum, with $\chi^2_{red} \approx .37$. The dark matter spatial profile is Einasto with $\alpha = 0.17$. Black dashed lines are the background prediction for a model with $\gamma_e = 2.55$ and $r_B = 8.5$ kpc. Colored dashed lines give the contributions from new sources, while colored solid lines give the total signal from new source and background.

can provide better fits and alleviate the problems of each individual scenario. However, this extra freedom means that fits are much less constrained. For the fits presented here, errors in the spectra are much larger than the spectra themselves and are not shown.

To avoid the large normalization factors necessary for dark matter decay or pulsars to fit the data, we only consider linear combinations that include dark matter annihilation. Thus enough synchrotron can easily be produced with lower magnetic fields. We also fix α to the middle value of $\alpha = 0.17$.

Generally, the power from dark matter annihilation at 10-100 GeV produces sufficient synchrotron for a large fraction of the WMAP signal, while the power at 100-5000 GeV produces part of the gamma ray signal. Decaying dark matter or pulsars can then freely produce the rest of the local cosmic ray signal without significantly

impacting the predictions from near the galactic center. Because decaying dark matter and pulsars do not give very different answers we don't show the fit to all three.

Fig. 10 is the fit to annihilation and pulsars. The fit to annihilation and decay is very similar, and thus not shown. Fig. 11 is the fit to annihilation and a modification of the background primary electrons. This case is perhaps the most realistic of the possibilities, if a new source is allowed. There is an unusual spike at low energies which just allows the primary electrons to more precisely match the features in the Fermi low energy cosmic ray data, without overproducing any other signal. We have not shown a fit to a combination of pulsars and a modification of the primary electrons because, as mentioned above, for both scenarios it was extremely difficult to produce the haze. A linear combination of the two would not alleviate this problem.

V. CONCLUSIONS

We have thoroughly examined the annihilating dark matter, decaying dark matter, and pulsar explanations of the recent anomalous cosmic ray, gamma ray, and synchrotron signals. We investigated whether each scenario can fit all of these data simultaneously. Our analysis is independent of the particle physics or pulsar model details of each scenario and only depends on the spatial profiles and background models. We determined the necessary injection spectrum of electrons and positrons in each case in order to reproduce the data, including the effects of different background models, propagation models, and solar modulation.

Though decaying dark matter is the best fit, the large normalization factors suggest that it will be difficult to find a fully self-consistent model with decaying dark matter that can explain the data, without changing some aspect of our model by a large amount. In particular, it may be necessary to find either a radiation field model with roughly twice as much starlight to produce enough IC, a rather large magnetic field of $33\mu G$ in the Galactic center, enormous amounts of low energy electrons or gamma rays injected, a much steeper dark matter profile, or a combination of these.

Pulsars give the worst fit; the disk-like profile makes it nearly impossible to produce both the gamma ray and synchrotron signals. Much like the decaying dark matter case, this suggests that dramatic re-assessments of backgrounds and models are necessary to find a self-consistent interpretation of the data.

Annihilating dark matter, however, has self-consistent fits with conventional astrophysical background models. Though we had to choose a somewhat shallower dark matter halo profile with Einasto $\alpha = 0.22$, it is still within the current range of profiles found by simulations. Furthermore, we can satisfy the gamma ray constraints from

the GC. The boost factors are $\sim 70/f_E$, which at first seems much lower than the boost factors of ~ 1000 often used in the literature. Several factors enter in this difference: our use of the updated $\rho_0 = .4 \text{ GeV/cm}^3$ rather than $\rho_0 = .3 \text{ GeV/cm}^3$ [59], the relatively hard spectrum allowed by the fit, and our assumption that the cutoff of the spectrum is m_χ . Given these factors, our result of $\sim 70/f_E$ is typical of the models discussed in the introduction of this paper. However, the shape of the spectrum, combined with a lack of π^0 or \bar{p} production, may still be difficult to achieve in current particle physics models of dark matter.

Our results should be regarded as qualitative guidelines to injection spectra. The specifics will necessarily change as both Galactic models and data are refined. The WMAP “haze” data will be superseded by data from Planck [65], while data from Fermi and PAMELA will improve. In addition, cosmic ray data from AMS-02 [66] may also soon be available. If the data does not change substantially, and if current models indeed describe Galactic propagation and interactions, then the qualitative results of this paper will remain valid.

ACKNOWLEDGMENTS

We are grateful to Ilias Cholis, Marco Cirelli, Tracy Slatyer, and Neal Weiner for helpful discussions and comments on this paper. The computations in this paper were run on the Odyssey cluster supported by the FAS Research Computing Group at Harvard. TL is supported by an NSF graduate fellowship. DPF is partially supported by NASA Theory grant NNX10AD85G. This research made use of the NASA Astrophysics Data System (ADS) and the IDL Astronomy User’s Library at Goddard.⁵

-
- [1] L. Latronico, for the Fermi LAT Collaboration(2009), arXiv:0907.0452 [astro-ph.HE].
 - [2] L. Latronico, for the Fermi LAT Collaboration, “The Fermi-LAT Measurement of the Primary Cosmic Ray Electron Spectrum Between 5 GeV and 1 TeV,” (November 2009), presented at the Fermi Symposium, Washington DC.
 - [3] M. Pesce-Rollins, for the Fermi-LAT Collaboration(2009), arXiv:0912.3611 [astro-ph.HE].
 - [4] N. Gehrels and P. Michelson, *Astroparticle Physics* **11**, 277 (Jun. 1999).
 - [5] O. Adriani *et al.* (PAMELA), *Nature* **458**, 607 (2009), arXiv:0810.4995 [astro-ph].
 - [6] G. Dobler and D. P. Finkbeiner, *Astrophys. J.* **680**, 1222 (2008), arXiv:0712.1038 [astro-ph].
 - [7] G. Dobler, D. P. Finkbeiner, I. Cholis, T. R. Slatyer, and N. Weiner(2009), arXiv:0910.4583 [astro-ph.HE].
 - [8] B. Katz, K. Blum, and E. Waxman(2009), arXiv:0907.1686 [astro-ph.HE].
 - [9] P. Blasi, *Phys. Rev. Lett.* **103**, 051104 (2009), arXiv:0903.2794 [astro-ph.HE].
 - [10] P. Blasi and P. D. Serpico, *Phys. Rev. Lett.* **103**, 081103 (2009), arXiv:0904.0871 [astro-ph.HE].
 - [11] P. D. Serpico, *Phys. Rev.* **D79**, 021302 (2009), arXiv:0810.4846 [hep-ph].
 - [12] O. Adriani *et al.*, *Phys. Rev. Lett.* **102**, 051101 (2009), arXiv:0810.4994 [astro-ph].
 - [13] N. Arkani-Hamed, D. P. Finkbeiner, T. R. Slatyer, and N. Weiner, *Phys. Rev.* **D79**, 015014 (2009), arXiv:0810.0713 [hep-ph].
 - [14] I. Cholis, G. Dobler, D. P. Finkbeiner, L. Goode-nough, and N. Weiner, *Phys. Rev.* **D80**, 123518 (2009), arXiv:0811.3641 [astro-ph].
 - [15] M. Cirelli, R. Franceschini, and A. Strumia, *Nucl. Phys.*

⁵ Available at <http://idlastro.gsfc.nasa.gov>

- B800**, 204 (2008), arXiv:0802.3378 [hep-ph].
- [16] M. Cirelli, M. Kadastik, M. Raidal, and A. Strumia, Nucl. Phys. **B813**, 1 (2009), arXiv:0809.2409 [hep-ph].
- [17] J. Mardon, Y. Nomura, D. Stolarski, and J. Thaler, JCAP **0905**, 016 (2009), arXiv:0901.2926 [hep-ph].
- [18] A. Arvanitaki *et al.*, Phys. Rev. **D79**, 105022 (2009), arXiv:0812.2075 [hep-ph].
- [19] C.-R. Chen, F. Takahashi, and T. T. Yanagida, Phys. Lett. **B671**, 71 (2009), arXiv:0809.0792 [hep-ph].
- [20] A. Ibarra, D. Tran, and C. Weniger, JCAP **1001**, 009 (2010), arXiv:0906.1571 [hep-ph].
- [21] J. Mardon, Y. Nomura, and J. Thaler, Phys. Rev. **D80**, 035013 (2009), arXiv:0905.3749 [hep-ph].
- [22] E. Nardi, F. Sannino, and A. Strumia, JCAP **0901**, 043 (2009), arXiv:0811.4153 [hep-ph].
- [23] J. T. Ruderman and T. Volansky(2009), arXiv:0907.4373 [hep-ph].
- [24] P.-f. Yin *et al.*, Phys. Rev. **D79**, 023512 (2009), arXiv:0811.0176 [hep-ph].
- [25] L. Gendeleev, S. Profumo, and M. Dormody, JCAP **1002**, 016 (2010), arXiv:1001.4540 [astro-ph.HE].
- [26] D. Hooper, P. Blasi, and P. D. Serpico, JCAP **0901**, 025 (2009), arXiv:0810.1527 [astro-ph].
- [27] D. Malyshev, I. Cholis, and J. Gelfand, Phys. Rev. **D80**, 063005 (2009), arXiv:0903.1310 [astro-ph.HE].
- [28] S. Profumo(2008), arXiv:0812.4457 [astro-ph].
- [29] H. Yuksel, M. D. Kistler, and T. Stanev, Phys. Rev. Lett. **103**, 051101 (2009), arXiv:0810.2784 [astro-ph].
- [30] J. P. Harding and K. N. Abazajian, Phys. Rev. **D81**, 023505 (2010), arXiv:0910.4590 [astro-ph.CO].
- [31] M. Kaplinghat, D. J. Phalen, and K. M. Zurek, JCAP **0912**, 010 (2009), arXiv:0905.0487 [astro-ph.HE].
- [32] T. Delahaye, R. Lineros, F. Donato, N. Fornengo, and P. Salati, Phys. Rev. **D77**, 063527 (2008), arXiv:0712.2312 [astro-ph].
- [33] T. Sjostrand, S. Mrenna, and P. Z. Skands, JHEP **05**, 026 (2006), arXiv:hep-ph/0603175.
- [34] V. Barger, Y. Gao, W. Y. Keung, D. Marfatia, and G. Shaughnessy, Phys. Lett. **B678**, 283 (2009), arXiv:0904.2001 [hep-ph].
- [35] L. Zhang, C. Weniger, L. Maccione, J. Redondo, and G. Sigl(2009), arXiv:0912.4504 [astro-ph.HE].
- [36] A. W. Strong, I. V. Moskalenko, and V. S. Ptuskin, Ann. Rev. Nucl. Part. Sci. **57**, 285 (2007), arXiv:astro-ph/0701517.
- [37] D. R. Lorimer(2003), arXiv:astro-ph/0308501.
- [38] A. W. Strong, I. V. Moskalenko, O. Reimer, S. Digel, and R. Diehl, Astron. Astrophys. **422**, L47 (2004), arXiv:astro-ph/0405275.
- [39] D. T. Cumberbatch, Y.-L. S. Tsai, and L. Roszkowski(2010), arXiv:1003.2808 [astro-ph.HE].
- [40] I. Cholis, L. Goodenough, D. Hooper, M. Simet, and N. Weiner, Phys. Rev. **D80**, 123511 (2009), arXiv:0809.1683 [hep-ph].
- [41] L. Stawarz, V. Petrosian, and R. D. Blandford, Astrophys. J. **710**, 236 (2010), arXiv:0908.1094 [astro-ph.GA].
- [42] I. V. Moskalenko, T. A. Porter, and A. W. Strong, Astrophys. J. **640**, L155 (2006), arXiv:astro-ph/0511149.
- [43] J. L. Han, R. N. Manchester, A. G. Lyne, G. J. Qiao, and W. van Straten, Astrophys. J. **642**, 868 (2006), arXiv:astro-ph/0601357.
- [44] T. R. Jaffe *et al.*(2009), arXiv:0907.3994 [astro-ph.GA].
- [45] M. Cirelli and P. Panci, Nucl. Phys. **B821**, 399 (2009), arXiv:0904.3830 [astro-ph.CO].
- [46] M. Papucci and A. Strumia(2009), arXiv:0912.0742 [hep-ph].
- [47] Fermi LAT Collaboration, “Lat background models,” <http://fermi.gsfc.nasa.gov/ssc/data/access/lat/BackgroundModels.html>.
- [48] M. Cirelli, P. Panci, and P. D. Serpico(2009), arXiv:0912.0663 [astro-ph.CO].
- [49] C.-R. Chen, S. K. Mandal, and F. Takahashi, JCAP **1001**, 023 (2010), arXiv:0910.2639 [hep-ph].
- [50] G. Hutsi, A. Hektor, and M. Raidal(2010), arXiv:1004.2036 [astro-ph.HE].
- [51] J. Alcaraz *et al.* (AMS), Phys. Lett. **B484**, 10 (2000).
- [52] H.E.S.S. Collaboration: F. Aharonian *et al.*, Astron. Astrophys. **508**, 561 (2009), arXiv:0905.0105 [astro-ph.HE].
- [53] L. J. Gleeson and W. I. Axford, Astrophys. J. **154**, 1011 (Dec. 1968).
- [54] T. Delahaye, J. Lavalle, R. Lineros, F. Donato, and N. Fornengo(2010), arXiv:1002.1910 [astro-ph.HE].
- [55] M. Simet and D. Hooper, JCAP **0908**, 003 (2009), arXiv:0904.2398 [astro-ph.HE].
- [56] C. G. T. Haslam, C. J. Salter, H. Stoffel, and W. E. Wilson, Astron. Astrophys. Supp. **47**, 1 (Jan. 1982).
- [57] T. Delahaye *et al.*, Astron. Astrophys. **501**, 821 (2009), arXiv:0809.5268 [astro-ph].
- [58] F. Sha, L. K. Saul, and D. D. Lee, in *Advances in Neural Information Processing Systems 15* (MIT Press, 2002) pp. 1041–1048.
- [59] R. Catena and P. Ullio(2009), arXiv:0907.0018 [astro-ph.CO].
- [60] J. F. Navarro *et al.*, Mon. Not. Roy. Astron. Soc. **349**, 1039 (2004), arXiv:astro-ph/0311231.
- [61] M. Kuhlen and D. Malyshev, Phys. Rev. **D79**, 123517 (2009), arXiv:0904.3378 [hep-ph].
- [62] I. Cholis and N. Weiner(2009), arXiv:0911.4954 [astro-ph.HE].
- [63] D. Malyshev, I. Cholis, and J. D. Gelfand(2010), arXiv:1002.0587 [astro-ph.HE].
- [64] C. A. Faucher-Giguere and A. Loeb, JCAP **1001**, 005 (2010), arXiv:0904.3102 [astro-ph.HE].
- [65] Planck(2006), arXiv:astro-ph/0604069.
- [66] AMS-02, <http://ams.cern.ch>.